Available online at www.sciencedirect.com

SciVerse ScienceDirect

Journal of the European Ceramic Society 32 (2012) 2129–2136

www.elsevier.com/locate/jeurceramsoc

Focused ion beam tomography of zirconia degraded under hydrothermal conditions

E. Jiménez-Piqué [a,b,*], A. Ramos [c], J.A. Muñoz-Tabares [a], A. Hatton [d,e], F. Soldera [d], F. Mücklich [d], M. Anglada [a]

[a] *Material Science and Metallurgical Engineering, Universitat Politècnica de Catalunya, Avda. Diagonal 647(ETSEIB) 08028 Barcelona, Spain*
[b] *Center for Research in Nanoengineering CRnE, Universitat Politècnica de Catalunya, C/Pascual i Vila 15, 08028 Barcelona, Spain*
[c] *Grup d'Enginyeria de Materials, Institut Químic de Sarrià – Universitat Ramon Llull, Via Augusta 390. 08017 Barcelona, Spain*
[d] *Department of Materials Science, Saarland University, Saarbrücken, Campus D3.3, 66123 Saarbrücken, Germany*

Received 11 November 2011; received in revised form 2 February 2012; accepted 9 February 2012
Available online 4 March 2012

Abstract

Three-dimensional tomography was performed on hydrothermal degraded zirconia by sequential focussed ion beam (FIB) sectioning and field emission scanning electron microscopy (FE-SEM) observation. By means of image analysis the distribution of microcracks produced under the surface was reconstructed and characterized.

Results show a microcrack network preferentially oriented parallel to the surface, and a gradient in microcrack density from the surface, which is coherent with other measurements that reveal a decrease in monoclinic phase. The elastic properties of the reconstructed volume are simulated, showing that the deterioration of mechanical properties of degraded zirconia can be mainly attributed to microcracking, with a minor contribution of the phase transformation.

Keywords: ZrO_2; Mechanical properties; Defects; Tomography; Fracture

1. Introduction

Zirconia ceramics have many applications due to their excellent mechanical properties as well as other functional properties such as low thermal conductivity or high ionic conductivity. The range of engineering applications is nowadays growing in a number of different fields: e.g. solid oxide fuel cells,[1] thermal barrier coatings,[2] as a tool in processing industry[3] or in biomaterial applications[4]; making zirconia one of the most used technical ceramics.

The excellent mechanical properties of zirconia, particularly its fracture toughness, are due to the tetragonal to monoclinic phase (*t–m*) transformation that occurs in presence of stress around a crack tip. This phase transformation is of martensitic type and induces a volume increase of around 4% which results in closure of an advancing crack. The metastable tetragonal phase is stabilized at room temperature with the addition of oxides, mainly yttria, calcia and ceria.

However, under the influence of humidity the material is susceptible to a spontaneous *t–m* phase transformation generally beginning on the surface due to the oxygen vacancy annihilation.[5] This phenomenon, known as aging, degradation or low temperature degradation, has received considerable attention in recent years because it was one of the causes of the premature failure of a batch of zirconia femoral heads for hip replacement.[6] Although these failures were due to a manufacturing error in the sintering stage, the results were the actual discard of zirconia as a femoral head material, regardless of its superior properties compared to other materials currently used, particularly metals. Nowadays, there is an increasing use of zirconia in many fields where low temperature

* Corresponding author at: Material Science and Metallurgical Engineering, Universitat Politècnica de Catalunya, Avda. Diagonal 647(ETSEIB) 08028 Barcelona, Spain. Tel.: +34 934011089; fax: +34 934016706.
E-mail address: emilio.jimenez@upc.edu (E. Jiménez-Piqué).
[e] A. Hatton (born Velichko), currently at J. D. Theile GmbH & Co. KG, Schwerte, Germany.

0955-2219/$ – see front matter © 2012 Elsevier Ltd. All rights reserved.
doi:10.1016/j.jeurceramsoc.2012.02.011

degradation may be a reliability issue in the long term, as in dental implants.[7]

It is then of capital importance to understand thoroughly the mechanisms of degradation in zirconia in order to assure long-term structural integrity and reliability in any application, and many efforts have been devoted to this goal.[8] It is now well established that degradation starts on the surface in contact with water around pores, cracks or other stress arising features. Once a single grain is transformed, the tetragonal to monoclinic transformation progresses to other grains by a nucleation and growth mechanism governed by a Mehl-Avrami-Johnson (MAJ) law.[9] As soon as the first pair of monoclinic variants has nucleated, the transformation spreads throughout the grain and it is stopped by the grain boundary, which acts as a barrier, unless both grains have a particular crystallographic orientation that favours transgranular transformation.[10] The strain associated with the formation of this first pair of monoclinic variants is dominated by the shear component and will be accommodated by grain boundary microcracking. This microcracking is induced by the high stress concentrations provided by deformation twins,[11] which have long been recognized as potentially important in crack nucleation. This process results in the generation of microcracks below the surface, which leads to a decrease in mechanical performance after the degradation has produced about 15% of monoclinic phase.[12]

Hydrothermal degradation can be detected by spectroscopic techniques such as X-ray Diffraction (XRD) or micro-Raman[13] or by microscopy techniques, such as scanning electron microscopy (SEM)[14] or particularly atomic force microscopy (AFM),[15] where the *t-m* phase transformation is detected by the uplift at the surface. Recently, Gaillard et al.[16] have also shown that instrumented nanoindentation is a valid tool to detect the degradation and the thickness of the degraded layer. This is a local technique and, therefore, can evaluate the properties in different areas of the material with a resolution of a few square micrometers. Moreover, it is a depth-sensitive technique, and, consequently, can characterize a material at different depths, unlike most scanning probe techniques, which usually work only at a fixed depth. This methodology has shown a good agreement with experimental results by micro-Raman and transmission electron microscopy (TEM).[12] However, as both microcracking and monoclinic phase are present at the same time, it is difficult to deconvolute their individual role in the drop of mechanical properties. It is worth mentioning that it is not trivial to estimate the mechanical properties of monoclinic phase because pure monoclinic zirconia is completely microcracked at room temperature and therefore it is not easy to measure the properties of a bulk crack-free sample.

Although some recent focussed ion beam (FIB) and TEM images have shown the shape and location of microcracks,[9,17] these are images of single cross section, and the information is partial. Therefore, there are still some questions open: (1) What is the geometry and orientation of these microcracks? (2) What is the density of the microcracks? and (3) Is it only the microcracking, which is responsible for the drop in mechanical properties, specially hardness and elastic modulus as measured by nanoindentation, or does the monoclinic phase have a significant contribution to this decrease in mechanical properties?

Therefore, the objective of this work is to characterize the microcrack network generated by hydrothermal degradation by FIB tomography, which allows a three dimensional reconstruction from sequential cross sections of a volume of several microns with a resolution of a few nanometres. This technique is an extremely powerful tool for characterization of microstructure[18,19] and damage of materials.[20] FIB tomography has higher resolution than X-ray tomography and larger analyzed volumes than with atom probe tomography. However, to apply FIB tomography for a bulk ceramic is a challenge, since charging effects may affect the stability of the process, having detrimental effects on the resolution of the technique. 3D image analysis is essential for the characterization of complex and spatially connected microstructures because it enables the acquisition of not only qualitative but also quantitative information of the microstructure. This quantitative information allows correlating the three-dimensional parameters to materials properties, such as density, hardness and elastic modulus.

2. Experimental

Commercially available powder of tetragonal polycrystalline zirconia, stabilised with 3% molar Y_2O_3, 3Y-TZP (TZ-3YSB-E, Tosoh corporation, Tokyo, Japan) were used. The powder was cold-pressed and sintered in order to obtain biomedical-grade zirconia according to ISO 13356:1997 [Implants for surgery—Ceramic materials based on yttria-stabilized tetragonal zirconia (Y-TZP)]. The materials were heat treated for 2 h at 1650 °C, in order to produce a duplex microstructure with larger grain size and larger microcraks, with a comparable behaviour to as sintered microstructure.[21]

Samples were cut into discs of approximately 2 mm thickness with a diamond blade circular saw and polished with diamond suspensions of decreasing particle size (30, 6, and 3 μm). After mechanical preparation, materials were treated for 1 h at 1200 °C in order to release any residual stresses. Finally, they were polished with colloidal silica. Hydrothermal degradation treatments were done in an autoclave at 134 °C and 1.8 bar in water vapour atmosphere for 14 h.

FIB tomography was done on a dual beam system Strata DB235 (FEI Company) following the procedure as described for instance in.[22] The dual beam system incorporates both a focused ion beam (FIB) and a field emission scanning electron microscope (FE-SEM) in a single instrument.

To avoid surface charging, samples were covered with a conductive layer deposited on the sample by sputtering gold during three minutes and were attached to the sample holder with adhesive copper tape and a drop of colloidal graphite. Once in the vacuum chamber, a platinum layer was deposited on the region of interest (ROI) so that the surface was protected from ion damage. First, platinum was deposited by electron beam induced deposition (EBID), since this techniques does not produce any damage at the material surface. After that, the sample was tilted 52° to have the surface perpendicular to the ion beam. Further deposition of platinum was done through ion beam induced

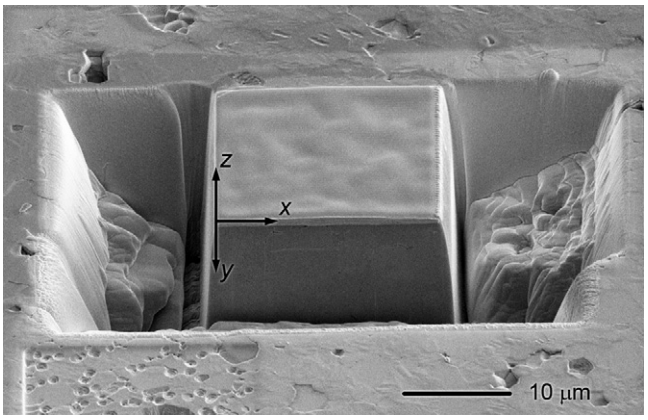

Fig. 1. SEM image of the trenches milled by FIB around the region of interest previously to sequential milling. Lateral trenches are produced in order to avoid redeposition of the material on the observed section.

deposition (IBID), which has a higher deposition rate. A trench was free milled in front of the ROI in order to have the XY plane accessible for image acquisition with the electron beam (see Fig. 1 for axes description). Further trenches were milled at the sides of the ROI avoiding shadowing effects and preventing that the redeposited material from the milling process hinders the imaging of the cross sections. The milling of the trench was done with higher ion currents (20 nA, 5 nA). Final polishing the serial sectioning is done with lower currents, in this case 500 pA.

The resolution of the FIB tomography is determined in the X and Y axes by the resolution of the SEM images. For the Z axes it is the distance between the successive slices. In this work the resolution of the tomography (equal to the voxel size) is: $x = 23$ nm, $y = 29$ nm and $z = 60$ nm. Resolution is different in X and Y axes due to the 52° tilting of the sample respect to the electronic column ($y = x/\sin 52°$).

Visualisation of the FIB nanotomography, alignment of the images and crack network reconstruction was performed with AMIRA software (Mercury Computer Systems).

In order to achieve the crack reconstruction, the images obtained after the tomography, were aligned and cropped in order to have a succession of images that show only the region of interest without artefacts (Fig. 2). Then, the cracks were manually segmented because no automated algorithm was found consistent enough to perform automatically the segmentation. The segmentation was performed mainly on the XY images and was completed with the help of the reconstructed images in YZ and ZX axis in order to correctly identify all microcracks.

Quantitative characterization of the crack network can be done with the help of such features as surface area (S), volume (V) and their densities. In 3D, the volume density (V_V) and surface density (S_V) were calculated as the volume and surface of the network divided by the total volume analyzed. In 2D images these basic characteristics (S_V and V_V) can also be determined from the sum of the perimeter (L_A) and area (A_A) of all single objects divided by the area of the image (here the objects are the two-dimensional sections of the three dimensional microcracks, according to the stereological equations:[23]

$$V_V = A_A \qquad S_V = \frac{4}{\pi} L_A \tag{1}$$

2D image analysis was performed in the three Cartesian orientations. Whereas frontal images (XY) are the segmented original images, axial (YZ) and sagittal (XZ) images were reconstructed from the segmented 3D crack network.

The quantitative microstructure analysis of the features was performed with the software A4i (Olympus) for the 2D-analysis and with MAVI (Fraunhofer ITWM, Kaiserlautern) for 3D-analysis.

The simulations of mechanical properties from the reconstructed 3D crack network were performed with the module Elastodict of the software GeoDict created in Fraunhofer ITWM. This program only allowed the use of isotropic voxels, thus the 3D image was respectively adjusted and the voxels size was set to 62.3 nm. After this transformation, the image was cropped in segments of five pixels in Y direction (parallel to the surface) and exported to GeoDict.

Table 1
Influence of morphological operations on the measurement of volume fraction (V_V), specific surface density (S_V), densities of the integral of mean (M_V) and total curvature (K_V).

	V_V ($\times 10^{-2}$)	S_V [μm^{-1}] ($\times 10^{-1}$)	M_V [μm^{-2}]	K_V [μm^{-3}]
	3D	3D	3D	3D
Output	2.17	6.57	3.06	−71.1
Closure	3.53	6.36	1.25	−16.5
Skeleton	1.14	6.49	8.89	−33.5

3. Results and discussion

As previously reported,[13,14] the material below the surface is severely damaged with a relatively high amount of microcraks, as seen in Fig. 2b. This microcracking is formed by shear deformation of the first martensitic plates produced in a partially transformed grain, which generates local tensile stresses in grain boundaries.

By sequential cross section of the material, the microcrack network can be reconstructed in three dimensions. After the segmentation of the original serial sections, the crack network is well recognizable. However, the quality of the segmentation does not allow further direct quantitative analysis.

In order to improve the obtained structure, closure and skeleton morphological operations were tested on a fraction of the reconstructed network and the results of the image analysis were compared (Table 1). The operation closure is the combination of two morphological operators: dilatation (which adds pixels to an object) and erosion (which removes pixels from an object). The closure helps filling small holes in objects or gaps between neighbouring objects. Skeletonisation reduces foreground regions in a binary image to a lower dimensional structure preserving the original connectivity. The skeleton image consists of thin (one pixel thickness) curves or surfaces,

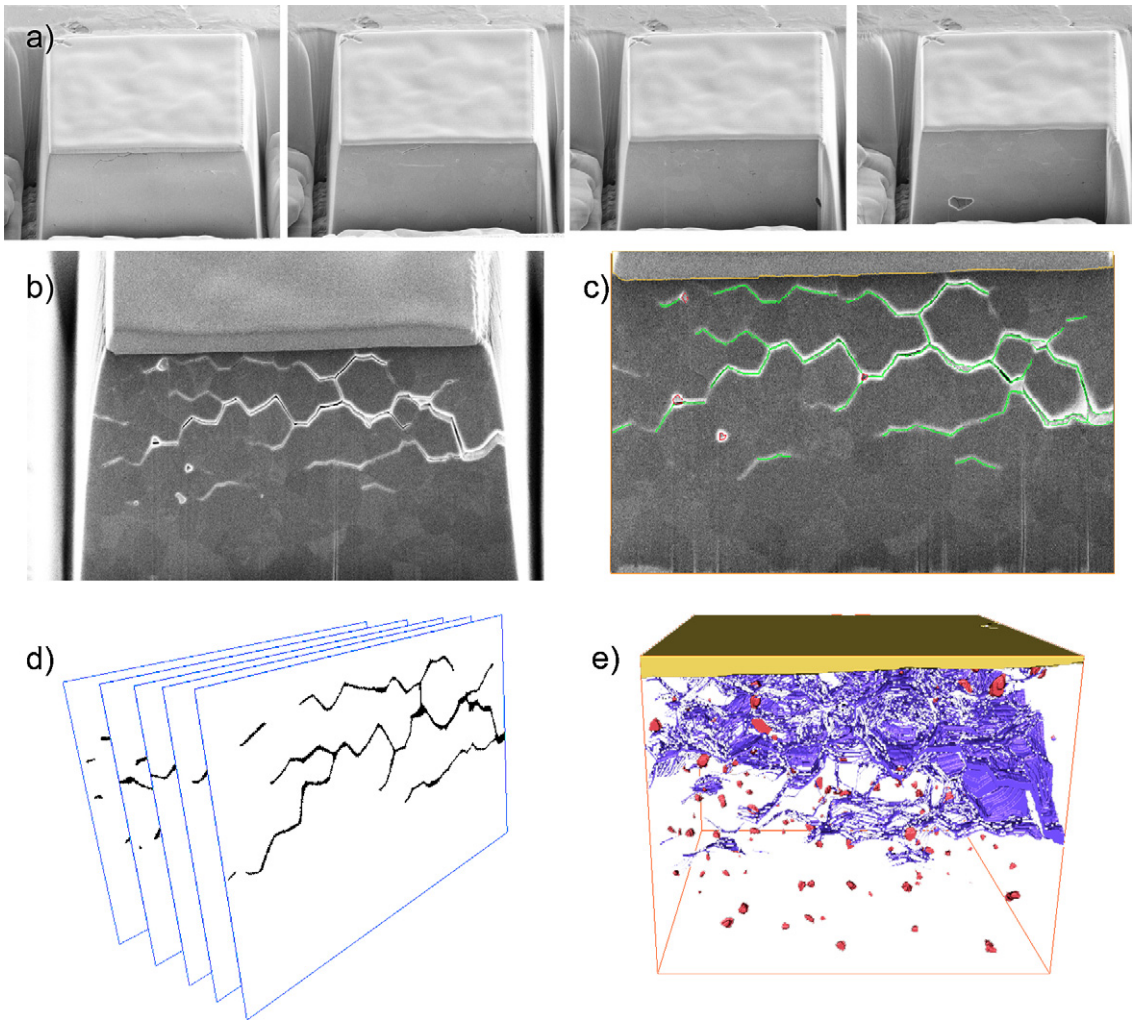

Fig. 2. Scheme of the tomographic imaging and reconstruction procedure: (a) example of four SEM images obtained sequentially by cross-sectioning with sequential cross-sectioning by Focused Ion Beam (b) cross section showing a detail of the microcrack network (c) segmentation of the microcracks and pores (d) series of segmented slices (e) reconstruction of the microcrack network (blue) and porosity (red, -small spheres-). (For interpretation of the references to color in this figure legend, the reader is referred to the web version of the article.)

having the same Euler number as the original object.[24] The morphological operations cause big changes in the volume fraction (V_V) of the cracks. The increase observed for the closure image is caused by the enhancement of connecting pixels after the operation. The decrease of volume fraction in the skeleton image is caused by the reduction of the structures to planes and lines. In contrast, the specific surface density (S_V) after each morphological operation is comparable to the output result. This main feature appears to be less sensitive to the morphological operations and therefore seems to be a good descriptor for this type of structures. The absolute value of the density of the integral of the total curvature (K_V which is a parameter that describes the spatial connectivity) increases after the skeleton morphological operation, which implies that this operation has caused the separation of the elements of the crack network, reducing the connectivity. This value decreases after the closure operation as the connectivity increases, leading to a better crack network reconstruction. Therefore, subsequent quantitative analysis of the crack network was performed after the closure morphological operation and considering the surface density as the main descriptor.

Fig. 3 presents three perspectives of the microcracks and pores as reconstructed from the FIB images where it can be observed that they appear to lay mostly parallel to the surface and are confined to a certain depth below the surface. In order to verify quantitatively this visual assessment, the orientation of the microcracks was analysed on 2D images in *YZ* and *XZ* directions. The orientation of each object on the plane was obtained from the orientation of the main axis of the ellipse adjusted to the particle, as shown in Fig. 4. From this figure, the preferential orientation of the microcraks parallel to the surface is clearly visible. The plane *YZ*, perpendicular to the surface (see also Fig. 1), shows a preferential distribution of microcrack surface parallel to the material surface, whereas the *XZ* plane (parallel to the material surface) shows no preferential distribution. Fig. 5 presents the orientation of the particles, where particles smaller than 4 pixels have been deleted in order to eliminate possible artefacts derived from the anisotropic pixel. Again, it is

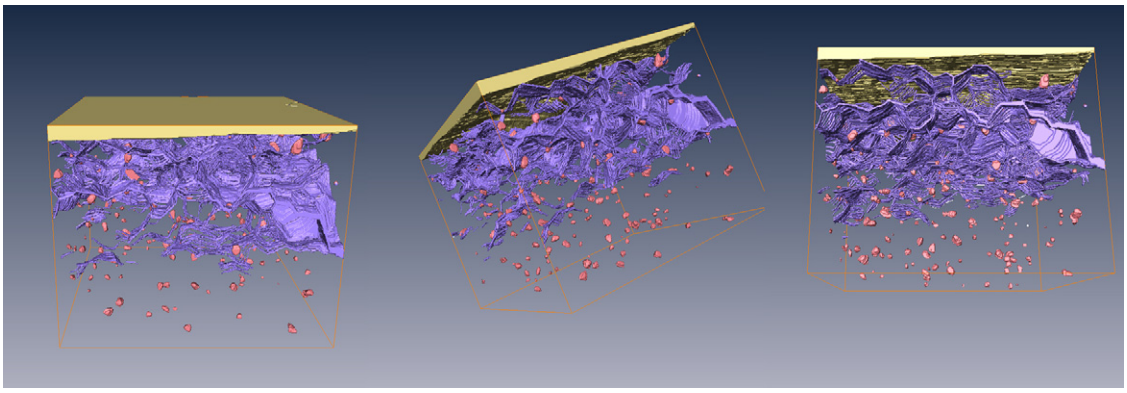

Fig. 3. Three different perspectives of the reconstructed volume of microcracks, showing platinum protective layer deposited previous to the tomography (yellow), microcracks network (blue) and pores (red, -small spheres-). (For interpretation of the references to color in this figure legend, the reader is referred to the web version of the article.)

seen how microcracks are preferentially oriented parallel to the surface (planes *YZ* and *XY*). From this preferential orientation it is expected that microcracks will not significantly contribute as channels for water penetration, and, consequently, will not accelerate the nucleation and growth of the monoclinic phase produced by hydrothermal degradation.

The average volume fraction of the microcracks in the *XY* and *YZ* planes, in the region where microcracks are present, was estimated to be $V_V = 0.03 \pm 0.01$ and the microcrack surface per unit volume was estimated to be $S_V = 0.5 \pm 0.2\ \mu m^{-1}$.

Previous studies[25,26] have shown that while performing a FIB tomography of indentations with cracks, these can open due to the relief of residual stresses due to the residual stress field produced by indentation. In the case of degraded zirconia, the *t–m* phase transformation produces residual stress which may not be fully accommodated by surface uplift and microcracking. In order to analyse the possible influence of the FIB tomography on the crack distribution, surface density of the crack network was determined in the *XY* (directly observed by SEM imaging). Fig. 6 shows the distribution of specific surface area (S_V) in the 2D *XY* images along the *X* axis (front to back). In this figure, a little increment of the surface density and a decrease of the amount of cracks at the back of the tomography are observed. This distribution corresponds to the observation on the SEM images that the cracks are visibly wider in the front of the analyzed volume than on the last images.

The opening of the cracks can be attributed to a stress release due to the lack of surrounding material caused by the trench erosion in front and on both sides of the analyzed volume. The back part of the sample is still in contact with the rest of the sample, which could explain that the cracks in that zone were more closed and resulting in a lower volume fraction. The surface area density should not be very sensitive to the opening of the cracks. This variation can be explained by the fact that the stress relieve initiates the opening of the small cracks in the front images. On the last images, these cracks are not seen and therefore do not contribute to the enlargement of the crack volume fraction or the specific surface area. This effect should be taken in consideration when analyzing connected network of cracks or pores under stress.

In Fig. 7 the volume fraction and microcrack surface per unit volume for the *XZ* plane (plane parallel to the surface) are presented as a function of the distance to the material surface. It is seen that most microcracks are located in a region nearby the surface, however the microcrack density is not constant, but presents a decreasing gradient with increasing depth. 75% of the measured cracks were comprised in a depth of 3.8 μm, which is slightly larger than the depth estimated by nanoindentation

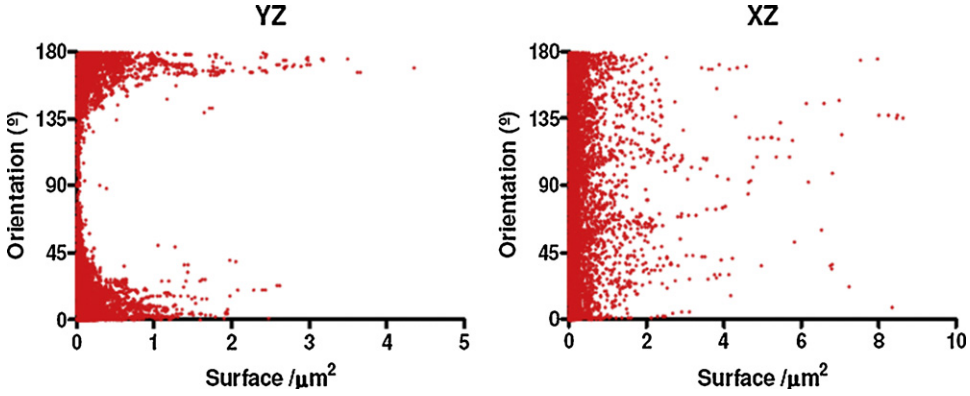

Fig. 4. Particle orientation distribution as a function of their surface area for the planes *YZ* and *XZ*. On the plane *YZ* preferable orientation parallel to the sample surface (0° and 180°) especially of the large particles can be observed. On the plane *XZ* no preferential orientation can be seen.

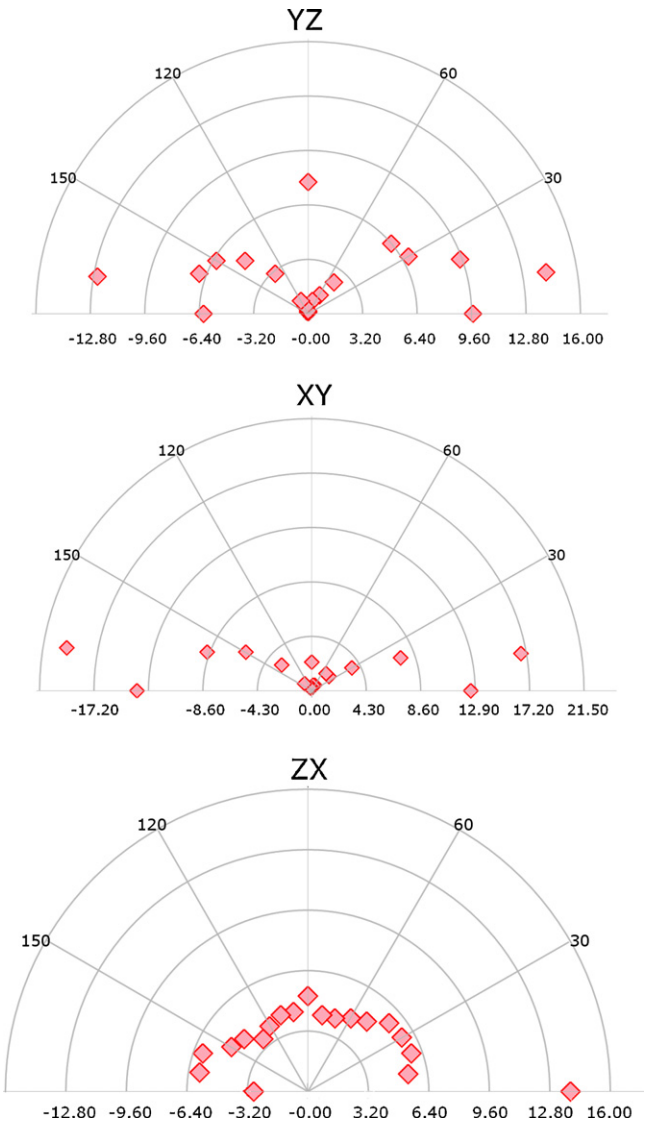

Fig. 5. Orientation of microcracks for the three different planes: *XY*, *YZ* and *ZX*. Crack surfaces show a preferential orientation in the *XY* and *YZ* planes. The microcracks are preferentially oriented parallel to the material surface.

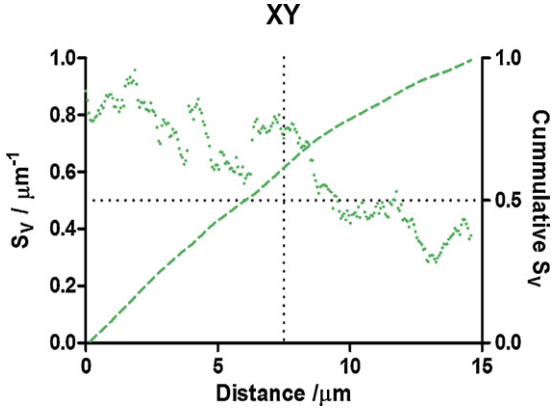

Fig. 6. Distribution of specific surface area (S_V) in the 2D *XY* images along the *Z*-axis (front to back).

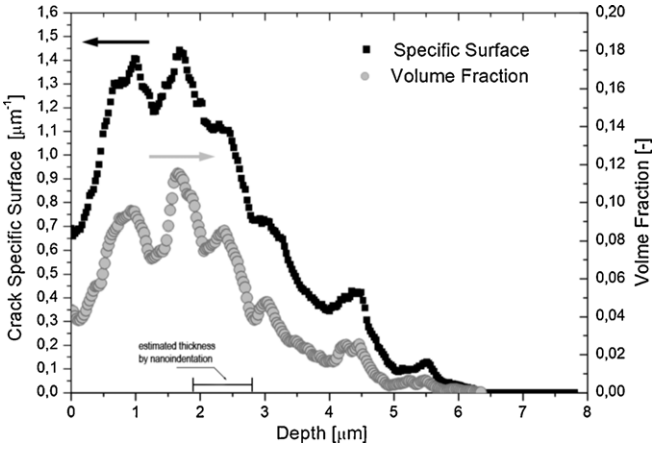

Fig. 7. Volume fraction and specific surface of microcracks obtained by the tomographic reconstructions as a function of depth. The estimated thickness by nanoindentation is also indicated.

(2.3 ± 0.4 µm).[16] This may be attributed to the fact that small microcracks which are detected by tomography will not have a significant effect in the mechanical response, and to the fact that the methodology for extracting the degraded layer from nanoindentation assumes a layer of degraded material with an abrupt transition to the healthy material. Despite this slight difference, nanoindentation correctly determines the depth where there is a maximum in the density of microcracks and where most of the microcracks are located (see Fig. 7). The gradient of microcrack density is coherent with a Mehl-Avrami-Johnson diffusion model, which has been measured for the monoclinic phase by Raman microscopy.[13]

The peaks that can be observed in Fig. 7 are related to the convolution of the gradient in density with the grain size of the material. In fact, if a Fourier analysis is performed in the data, a signal with 2.8 ± 0.8 mm periodicity can be extracted. This is similar to the grain size of the material, which consists of tetragonal grains of 1.37 µm and cubic grains of 3.84 µm mean diameter (cubic grains are 25% volume of the material).[27]

Nanoindentation tests calculated a value of elastic modulus of the degraded layer equal to $E_d = 185 \pm 15$ GPa. In this layer both microcracks and monoclinic phase (up to 80%) will coexist, and there is the question if the decrease in mechanical properties is due to the monoclinic phase or to the microcracks. In order to solve this, once the tomography is performed the elastic modulus of the reconstructed volume is calculated with the software GeoDict, which analyzes the elastic properties of composite microstructures, in our case cracks ($E_{crack} = 0$ GPa) and healthy material ($E_{matrix} = 240$ GPa). The average Young's modulus obtained by the software is 208 ± 80 GPa. The elastic modulus calculated at different depths is presented in Fig. 8, together with the values of Young's modulus obtained by nanoindentation. It should be taken into account that is a simplified model, however, it is observed that there is a good agreement between the elastic modulus measured by nanoindentation and the one calculated from the reconstructed microstructure in 3D. At large depths, the calculated elastic modulus increases due to the decrease in microcracks. For the case of the nanoindentation

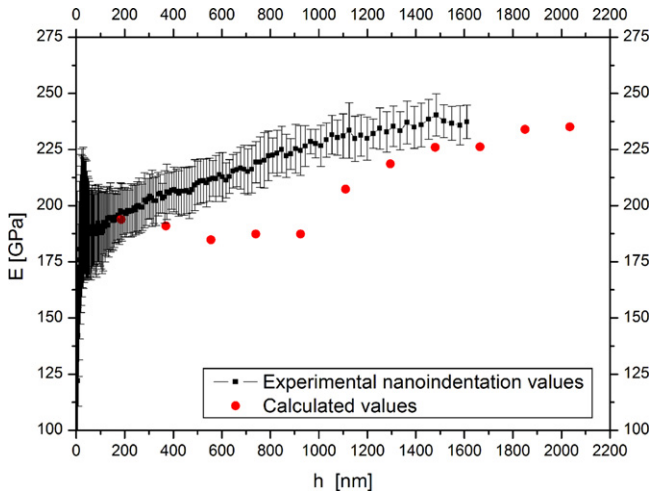

Fig. 8. Young's modulus obtained by nanoindentation and calculated through an elastic analysis of the reconstructed volume using the software GeoDict.

data there is also the increasing contribution of the substrate, which will contribute to the overall elastic response, as elastic fields in nanoindentation are deeper than the penetration depth.

In addition, the elastic modulus was also estimated by using a model for indentation response of porous zirconia.[28] The measured volume fraction of microcracks was used as a volume fraction of pores, and a form factor of around 50 was assumed for this porosity. The elastic modulus calculated was 192 GPa, in good agreement with the value obtained by nanoindentation, confirming thus that the decrease of mechanical properties in low temperature degraded zirconia can be mostly attributed to microcracking and not to monoclinic phase.

4. Conclusions

The focused ion beam tomography has allowed the three dimensional reconstruction of the microcrack network produced during hydrothermal degradation. According to image analysis results, closure morphological operation has been shown to be the best option for improving quality of the segmentation, and the surface density is the most robust parameter in order to quantify the microcrack distribution. Moreover, the developed reconstruction and characterization procedure provides solid basis for further correlations of the microstructural parameters with material properties of degraded zirconia and other microcracked solids.

It has been shown that microcracks are preferentially oriented parallel to the surface, and are not connected with the surface. In addition, the density of microcraking decreases with depth, in agreement with the decrease of monoclinic phase content measured by other techniques, coherent with a diffusion model.

Modelling the elastic properties of the measured microcrack network has shown that the elastic decrease measured by nanoindentation can be mostly attributed to the loss in stiffness produced by the microcracks. Therefore, the decrease in mechanical performance in degraded zirconia is largely due to microcraks, and that the monoclinic phase has similar elastic properties than the tetragonal phase.

Acknowledgments

The authors would like to acknowledge the financial support provided by the Ministerio de Ciencia e Innovación (MICINN) of Spain through project MAT2008-03398 F. Soldera and F. Mücklich thank the EFRE Funds of the European Commission for support of activities within the AME-Lab project.

References

1. Morales M, Roa JJ, Capdevila XG, Segarra M, Piñol S. Mechanical properties at the nanometer scale of GDC and YSZ used as electrolytes for solid oxide fuel cells. *Acta Mater* 2010;**58**:2504–9.
2. Gaillard Y, Jimenez-Pique E, Anglada M. Scale dependence of the Young's modulus measured by nanoindentation in columnar YSZ EB-PVD thermal barriers coatings. *Phil Mag* 2006;**86**:5441–51.
3. Kara A, Tobyn MJ, Stevens R. An application for zirconia as a pharmaceutical die set. *J Eur Ceram Soc* 2004;**24**:3091–101.
4. Piconi C, Maccauro G. Zirconia as a ceramic biomaterial. *Biomaterials* 1999;**20**:1–25.
5. Guo X. Hydrothermal degradation mechanisms of tetargonal zirconia. *J Mater Sci* 2001;**36**:3737–44.
6. Chevalier J, Gremillard L, Virkar AV, Clarke DR. The tetragonal-monoclinic transformation in zirconia: lessons learned and future trends. *J Am Ceram Soc* 2009;**92**:1901–20.
7. Cattani-Lorente M, Scherrer SS, Ammann P, Jobin M, Anselm Wiskott HW. Low temperature degradation of a Y-TZP dental ceramic. *Acta Biomaterialia* 2011;**7**:858–65.
8. Chevalier J. What future for zirconia as a biomaterial? *Biomaterials* 2006;**27**:535–43.
9. Chevalier J, Gremillard L, Deville S. Low-temperature degradation of zirconia and implications for biomedical implants. *Ann Rev Mater Res* 2007;**37**:1–32.
10. Deville S, Guenin G, Chevalier J. Martensitic transformation in zirconia. Part II. Martensitic growth. *Acta Mater* 2004;**52**:5709–21.
11. Fischer F, Schaden T, Appel F, Clemens H. Mechanical twins, their development and growth. *Eur J Mech* 2003;**22**:709–26.
12. Muñoz-Tabares JA, Jiménez-Piqué E, Anglada M. Subsurface evaluation of hydrothermal degradation of zirconia. *Acta Mater* 2011;**59**:473–84.
13. Muñoz-Tabares JA, Anglada M. Quantitative analysis of monoclinic phase in 3Y-TZP by Raman spectroscopy. *J Am Ceram Soc* 2010;**936**:1790–5.
14. Kim Y, Jung C, Park J. Low temperature degradation of yttria-stabilized tetragonal zirconia polycrystals under aqueous solutions. *J Nucl Mater* 1994;**209**:326–31.
15. Deville S, Gremillard L, Chevalier J, Fantozzi G. A critical comparison of methods for the determination of the aging sensitivity in biomedical grade yttria-stabilized zirconia. *J Biomed Mater Res B* 2005;**72**:239–45.
16. Gaillard Y, Jiménez-Piqué E, Soldera F, Mücklich F, Anglada M. Quantification of hydrothermal degradation in Zirconia by nanoindentation. *Acta Mater* 2008;**56**:4206–16.
17. Marro FG, Chintapalli R, Hvizdos P, Soldera F, Mücklich F, Anglada M. Study of near surface changes in yttria-doped tetragonal zirconia after low temperature degradation. *Int J Mater Res* 2009;**100**:92–6.
18. Velichko A, Mucklich F. Microstructure tomography – an essential tool to understand 3D microstructures and degradation effects. *Adv Sol State Phys* 2009;**48**:331–42.
19. Velichko A, Holzapfel C, Siefers A, Schladitz K, Mücklich F. Unambiguous classification of complex microstructures by their three-dimensional parameters applied to graphite in cast iron. *Acta Mater* 2008;**56**:1981–90.
20. Jeanvoine N, Holzapfel C, Soldera F, Mücklich F. Microstructure characterisation of electrical discharge craters using FIB/SEM dual beam techniques. *Adv Eng Mater* 2008;**10**:973–7.

21. Gaillard Y, Anglada M, Jimenez-Pique E. Nanoindentation of yttria-doped zirconia: effect of crystallographic structure on deformation mechanisms. *J Mater Res* 2009;**24**:719–27.
22. Soldera F, Lasagni FA, Mücklich F. Nano characterization of structures by focused ion beam (FIB) tomography. In: Lasagni F, Lasagni A, editors. *Fabrication and characterization in the micro-nano range, advanced structured materials 10*. Berlin/Heidelberg: Springer-Verlag; 2011., ISBN 978-3-642-17781-1 p. 171–200.
23. Ohser J, Mücklich F. *Statistical analysis of microstructures in materials science*. UK: John Wiley and Sons Ltd; 2000.
24. Russ JC, Dehoff RT. *Practical stereology*. 2nd ed. New York: Plenum Press; 2000.
25. Elfallagh F, Inkson BJ. 3D analysis of crack morphologies in silicate glass using FIB tomography. *J Eur Ceram Soc* 2009;**29**:47–52.
26. Elfallagh F, Inkson BJ. Evolution of residual stress and crack morphologies during 3D FIB tomographic analysis of alumina. *J Microsc* 2008;**230**:240–51.
27. Casellas D, Cumbrera FL, Sanchez-Bajo F, Forsling W, Llanes L, Anglada M. On the transformation toughening of Y-ZrO_2 ceramics with mixed Y-TZP/PSZ microstructures. *J Eur Ceram Soc* 2001;**21**:765–77.
28. Luo J, Steven R. Porosity-dependence of elastic moduli and hardness of 3Y-TZP ceramics. *Ceram Int* 1999;**25**:281–6.